10-1-2023

Experiments and modelling of biomass pulverisation in swirling and non-swirling bluff body-stabilised turbulent annular flows

Syed Ehtisham Gillani
Edith Cowan University

Yasir M. Al-Abdeli
Edith Cowan University

Zhao F. Tian

10.1016/j.powtec.2023.118855
Gillani, S. E., Al-Abdeli, Y. M., & Tian, Z. F. (2023). Experiments and modelling of biomass pulverisation in swirling and non-swirling bluff body-stabilised turbulent annular flows. Powder Technology, 428, 118855. https://doi.org/10.1016/j.powtec.2023.118855

Powder Technology 428 (2023) 118855

Contents lists available at ScienceDirect

Powder Technology

journal homepage: www.journals.elsevier.com/powder-technology

Experiments and modelling of biomass pulverisation in swirling and non-swirling bluff body-stabilised turbulent annular flows

Syed Ehtisham Gillani [a,*], Yasir M. Al-Abdeli [a], Zhao F. Tian [b]

[a] School of Engineering, Edith Cowan University, Joondalup, WA 6027, Australia
[b] School of Electrical and Mechanical Engineering, The University of Adelaide, Adelaide, SA 5005, Australia

HIGHLIGHTS

- Pulverised biomass-laden turbulent jets investigated under confinement.
- Particle Image Velocimetry and Discrete Phase Model used to resolve particle flow and dispersion.
- Annular jet recirculates biomass particles over the bluff-body and disperses them downstream.
- Addition of swirl significantly enhances particle entrainment and lateral dispersion.
- For the same particle loading, low *Re* of carrier gas promotes upstream mixing and downstream particle dispersion.

GRAPHICAL ABSTRACT

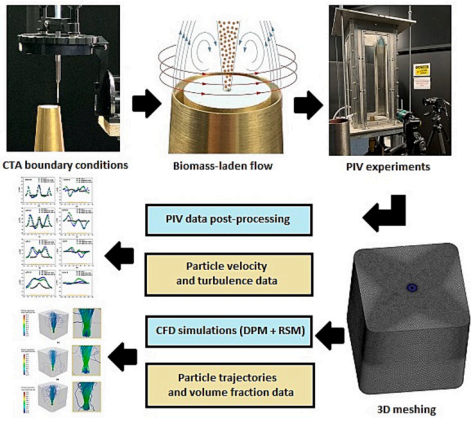

ARTICLE INFO

Keywords:
Biomass
Particle-laden turbulent flow
Particle image velocimetry
Discrete phase model
Swirl

ABSTRACT

Deeper insights into particle loading have practical significance in applications particularly when this affects fuel-oxidiser mixing and flame stabilisation, as occurs in pulverised fuel (biomass) combustion systems. The underlying particle flow and dispersion characteristics not only play a crucial role in controlling overall combustion performance but can also impact emissions. A fundamental understanding of particle flow dynamics and dispersion behaviour for raw pulverised biomass, under non-swirling and swirling conditions need further systematic investigation to better understand the interplay between swirling and non-swirling bluff-body stabilised recirculation zones and particles emitted from a centralised jet. This work uses Particle Image Velocimetry (PIV) with three-dimensional multi-phase simulations based on the Discrete Phase Model (DPM) and Reynolds Stress Model (RSM) to investigate the flow and dispersion characteristics in confined flows typical of many practical combustors. Raw pulverised biomass-laden is introduced through a central turbulent jet (Re_j = 4500 and 7800) and also subjected to turbulent annular flows (Re_s = 35,500), both non-swirling (S = 0) and swirling conditions (S = 0.3). Simulations are first validated against Constant Temperature Anemometry (CTA) resolved inlet boundary conditions and flow field PIV data under similar conditions.

* Corresponding author.
E-mail address: segillan@our.ecu.edu.au (S.E. Gillani).

https://doi.org/10.1016/j.powtec.2023.118855
Received 1 April 2023; Received in revised form 26 July 2023; Accepted 28 July 2023
Available online 29 July 2023

Results show that when a pulverised biomass-laden central jet interacts with a surrounding turbulent annular flow (non-swirling, swirling) the presence of a bluff-body based recirculating zone (BB-RZ) leads to biomass particle entrainment (pick up) and their recirculation over the bluff-body before being dispersed further downstream. Under non-swirling conditions, a significant 35% decrease in the mean particle axial velocity is measured coupled with an even more substantive 177% increase in turbulent fluctuation along the centreline. These findings are indicative of intense upstream ($x/D \approx 0.64$) turbulent mixing and more intense particle dispersion into a BB-RZ. For swirling annular flow conditions near the end of the BB-RZ, the interaction between a biomass-laden central jet and the annular flow is comparatively weaker in the upstream region relative to non-swirling conditions. However, swirl significantly enhances downstream particle dispersion and lateral spread as reflected by a 254% hike in the mean particle radial velocity. Numerical predictions show that for the same particle loading ratio, but different (higher and lower) Reynolds number of a central particle-laden jet (i.e., the carrier gas), the conditions at relatively lower central jet Reynolds number allow better particle recirculation in BB-RZ as well as enhancing downstream lateral particle dispersion and entrainment, compared to a higher Reynolds number in the central jet. Outcomes from this investigation may have implications on the design and operation of pulverised (solid) fuel combustors if operated on renewably sourced biomass rather than traditional fossil fuels.

1. Introduction

The use of particle-laden turbulent gaseous flows is prevalent in various industrial applications such as coal-fired power plants, circulating fluidised bed reactors, entrained flow gasifiers, cyclone separators, etc. [1–4]. Recently, there has been a growing interest in incorporating biomass (particularly pulverised) in major power generation systems to minimise fossil fuel usage and encourage carbon-neutral low-emission fuel sources [5–8]. Pulverised biomass combustion is primarily non-premixed where key parameters such as fuel-oxidiser mixing, flame stabilisation, recirculation of hot reaction products and pollutant emissions are closely linked to the underlying velocity field and flow dynamics [9–11]. Fundamental understanding of the intrinsic flow field, particle dispersion and aerodynamics associated with pulverised raw biomass is still in the early stage despite the research undertaken on pulverised biomass combustion [7,8,12,13], coal-biomass co-firing [14–16] and particle-laden turbulent flows [17–19]. Many practical non-premixed (high power) combustion systems are based on swirl so as to promote higher turbulence and enhance fuel-oxidiser mixing in the reaction zone [9,20,21]. The use of pulverised biomass particles in such turbulent swirling flows further elevates the complexity of flow as the solid particles (irregular, non-spherical and fibrous in nature) [22,23] interact with the gas phase, thereby potentially affecting shear layers and being subject to the intrinsic flow structures induced through recirculation. The present study uses laser diagnostics and numerical modelling to investigate pulverised (powdered) biomass-laden jets, with particular focus on resolving the flow field, particle dispersion behaviour in both swirling and non-swirling jets when operated under confinement, as would occur in most high power practical combustors. As such, the work is essential in providing an insight into the opportunities and challenges associated with using (renewable) biomass fuels to supplement or replace traditional solid (fossil) fuels used in thermal power plants.

Although numerous studies have already investigated the multiphase flow field and particle dynamics associated with particle-laden turbulent flows [24,25], these fall short of the present study. Most earlier works either used spherical glass beads [19,26] to mimic particles or focused on pulverised coal based combustion systems [27–29], with very limited data available on the characteristics of such systems when operated on pulverised biomass. Fang et al. [26] experimentally investigated particle-laden gaseous flows in the upstream of a co-axial nozzle. The entrainment behaviour of particles in the near-field was found to be influenced by particle size, mass flow rate and diameter of the central tube through which particles are ejected. The influence of particle size, mass flow rate and central tube diameter on the entrainment was studied, however, only non-swirling flows with glass beads (as particles) having much higher density (2490 kg/m3) than pulverised biomass were used. Recently, Liang et al. [19] used PDA (Particle Dynamic Analyser) to measure gas and dispersed phase mean velocity and turbulence data for particle-laden turbulent reacting flows but measurements were conducted only at four axial positions and lacked overall flow field and particle dispersion characteristics. In terms of the modelling of pulverised biomass-laden flows, Elorf et al. [13,30] conducted series of numerical investigations using RANS (Reynold's Averaged Navier Stokes) and DPM (Discrete Phase Model) to study the impact of swirl on flow, combustion characteristics, and flame dynamics of pulverised biomass (olive waste) in a co-axial burner configuration. However, unlike the present study, that earlier research did not use pulverised biomass for model validation but with data from pulverised coal. Additionally, and despite implementing a DPM, particle motion or trajectories were not discussed. As such, the present study addresses these shortcomings. Göktepe et al. [31] conducted cold flow PIV (Particle Image Velocimetry) based experiments to investigate the effect of swirl on 112–160 μm sized pulverised biomass (pine) particles in a swirl-stabilised burner. It was found that regions of heavy particle concentration caused deceleration in gas phase velocities whereas swirl generated centrifugal forces considerably increased particle dispersion. Though an important discussion on biomass particle behaviour under swirl was provided, the interaction of particles with underlying annular flow structures (recirculation zones) was not addressed. Similarly, Geshwindner et al. [32] investigated the particle velocity field, respective slip velocities and local particle Reynolds number of pulverised biomass-laden turbulent jets using multiphase PIV in combination with novel pulse picking methodology. However, their study was based on simple axisymmetric biomass-laden jet only with no annular or co-axial jets around to replicate complex practical flows. These geometrical considerations can be integral to lab-based research burners and practical combustors, particularly those featuring swirl [33]. Recently, Wan et al. [34] used Discrete Element Method (DEM) based CFD simulations to investigate particle-laden coaxial swirling flows in an industrial-scale annular pipe. The impact of geometric parameters was studied and found that dispersion of particles varies directly with the vane angle and diameter of the swirler. Conversely, an inverse correlation was observed with the length of the swirler. In summary, the majority of works discussed above either investigated non-biomass based particle-laden flows or were studied in a co-axial or single jet environment. These have been no attempt to systematically investigate the flow and dispersion characteristics of raw pulverised biomass under both non-swirling and swirling turbulent jet conditions with an annular geometry.

Driven by the significant research gaps which have been highlighted in the existing body of literature on particle laden flows, the present paper uses time-averaged 2D (planar) PIV along with 3D RANS, featuring DPM based multiphase simulations, to resolve particle flow and dispersion characteristics. Pulverised raw biomass is used throughout under turbulent jet conditions ($Re_j = 4500$ and 7800). To provide a relative benchmark, the study first establishes the above in a

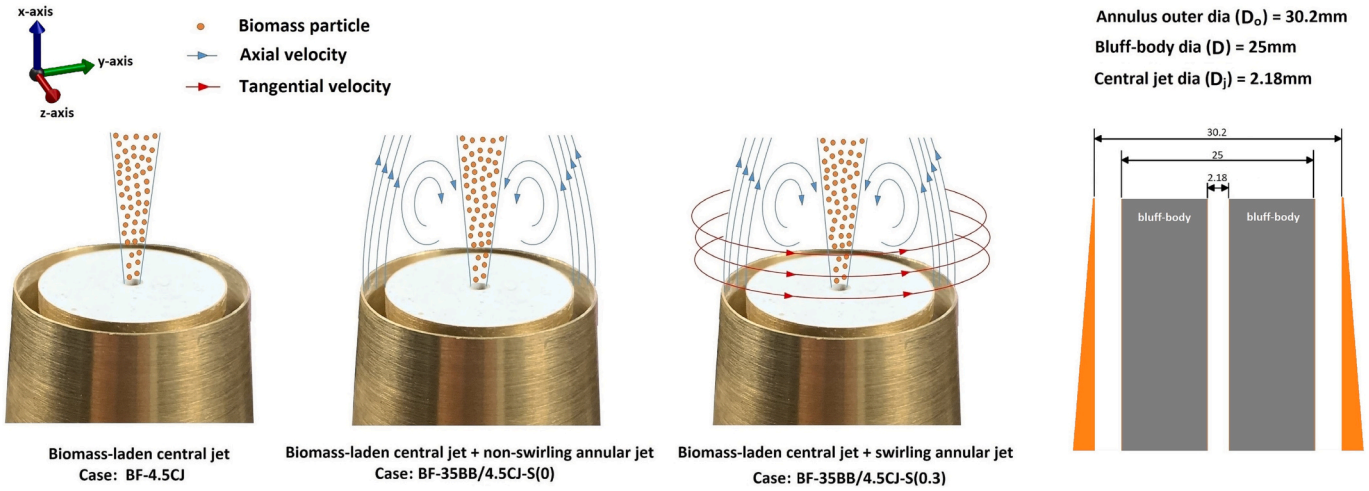

Fig. 1. Graphical representation of biomass-laden jet flow configurations with 2-D sectioned schematic of bluff-body and jets.

simple (axisymmetric, round) jet geometry before then moving to (more complex) annular flows operated under confinement, in both non-swirling (S = 0) and swirling (S = 0.3) conditions (Re_s = 35,500). Simulations utilise CTA resolved boundary conditions and are validated against PIV data. The contributions of this work are to:

- Establish (baseline) particle flow and dispersion characteristics of pulverised biomass-laden simple (axisymmetric, round) turbulent jets when subjected to turbulent annular flows.
- Investigate the effect of swirl on the velocity field and turbulence characteristics of pulverised jet operated using biomass.
- Numerically predict the effect of pulverised biomass loading and carrier gas Reynolds number on particle dispersion characteristics.

2. Methodology

2.1. Experimental setup

The test rig consists of a bluff-body stabilised swirl nozzle confined in an enclosure that is 310 mm × 310 mm (square) in cross-section and 700 mm high. The enclosure which has rounded internal corners also contains 580 mm × 160 mm fused silica glass windows on each side to provide optical access for laser diagnostics. More details on the enclosure are available in the literature [35,36]. The exit section of swirl nozzle is illustrated in Fig. 1(a) and consists has an outer diameter D_o of 30.2 mm, centrally-aligned bluff-body having a diameter D of 25 mm, a resultant blockage ratio D^2/D_O^2 of 0.69, and a central axisymmetric (round) jet with an inner diameter D_j = 2.18 mm. The nozzle is provided with dedicated axial (straight) and inclined tangential (inclined) ports to generate non-swirling and swirling flows, respectively.

2.1.1. Pulverised biomass-laden jet

The central jet from the ceramic-faced bluff-body which is shown in Fig. 1(b) generates a multiphase turbulent flow of dry air (carrier gas) and pulverised biomass particles. The volume flow rate of air was controlled by a duly calibrated flow meter (make: Influx; model: LV2S15-AI 27, accuracy: 2.5% full-scale) whereas, a motorised screw type particle dispenser (make: Barrell Engineering) was used to feed and control the mass flow rate of biomass particles. The particle dispenser has an integral pneumatic shaker (make: Cleveland Vibrator *Co.*; model: CVT) and an agitator (connected to its feed screw) to avoid particle agglomeration inside the (vertical) feed hopper. A variable speed drive (make: TECO; model: FM50) was used to control the feed rate of particles. The degree of multiphase interaction between biomass particles (solid) and air (gas phase) is characterised by particle loading ratio Φ_p [37] which is expressed in Eq. (1) as the ratio of mass flow rate of

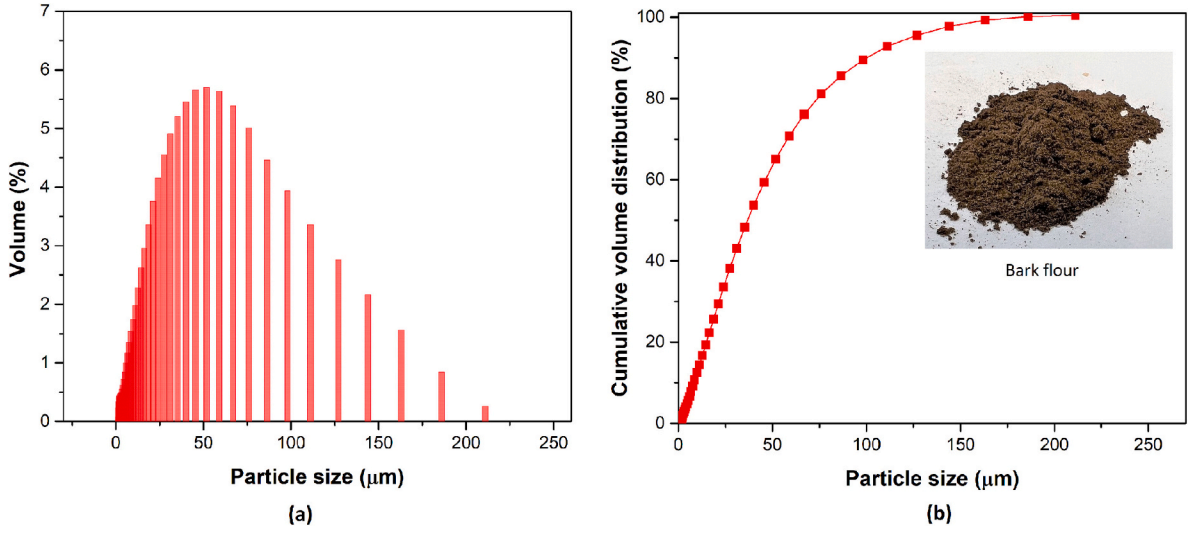

Fig. 2. Particle size distribution of pulverised biomass: (a) volume percentage and (b) cumulative volume distribution.

Table 1
Experimental flow settings for central and annular jets.

Jet type	Diameter (m)	Reynolds number	Flowrate (m^3/s)	Velocity (m/s)
Central jet	0.00218 (D_j)	4500 (Re_j)	1.2×10^{-4} ($Q_{j,a}$)	32.1 (U_j)
Annular jet	0.0302 (D_o) 0.0250 (D)	35,500 (Re_s)	8.46×10^{-3}(Q_s)	36.6 (U_s)

particles ($\dot{m_p}$) to that of carrier gas which is air ($\dot{m_a}$):

$$\Phi_p = \frac{\dot{m_p}}{\dot{m_a}} \quad (1)$$

The Reynolds number of the central jet (Re_j) is characterised by Eq. (2) in which $Q_{j,a}$ and ν represent the volume flow rate of air and kinematic viscosity of air (1.56×10^{-5} kg.m^{-1}.s^{-1}), respectively.

$$Re_j = \frac{4.Q_{j,a}}{\pi.D_j.\nu}. \quad (2)$$

2.1.2. Particle size distribution

The size distribution of the pulverised biomass (bark) particles was measured by using laser diffraction-based particle size analyser (make: Malvern Panalytical, UK; model: Mastersizer 3000). Particle size analysis was conducted using the general purpose volume-weighted analysis method built-in the OEM software. Fig. 2 presents the percentage volume and cumulative volume distribution of particles. The particle size distribution measurements were conducted in a size window of 0 to 250 μm. The percentage volume of particles at each size (diameter) is calculated by taking an average of 10 measured values.

2.1.3. Annular non-swirling/swirling jet

The gas phase turbulent jet emitting from the annulus is characterised by well-defined boundary conditions. Constant Temperature Anemometry (CTA) was used to resolve velocity data and characterise swirl number over the annulus. The CTA system (make: Dantec; model: 90 N10) features three data acquisition channels, designated for hot wire probes. A dual-wire miniature probe (model: 55P61) along with a temperature probe (model: 90C20) were used to measure the radial distribution of time-averaged axial and tangential velocity components over the annulus (at x/D = 0.2). The CTA probe was calibrated for velocity measurements using an automatic calibration system (make: Dantec; model: 90H10). Two standard calibrations were performed: (i) streamline calibration for a velocity range of 0.5 to 120 m/s and (ii) directional calibration for a range of −40 to 40 degrees to accommodate mean flow direction (resultant velocity angle [38]). A mechanical

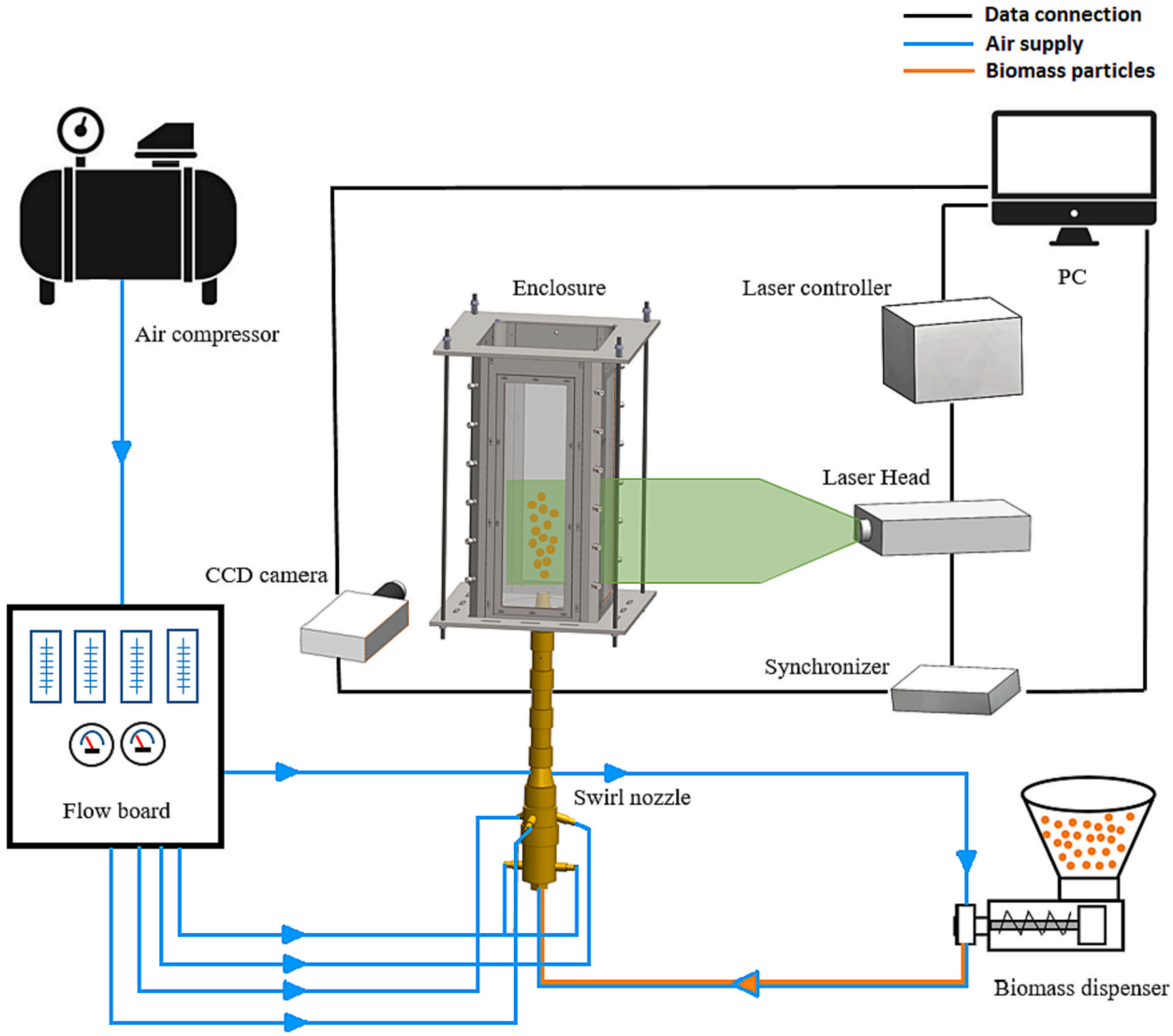

Fig. 3. Set-up for PIV experiments.

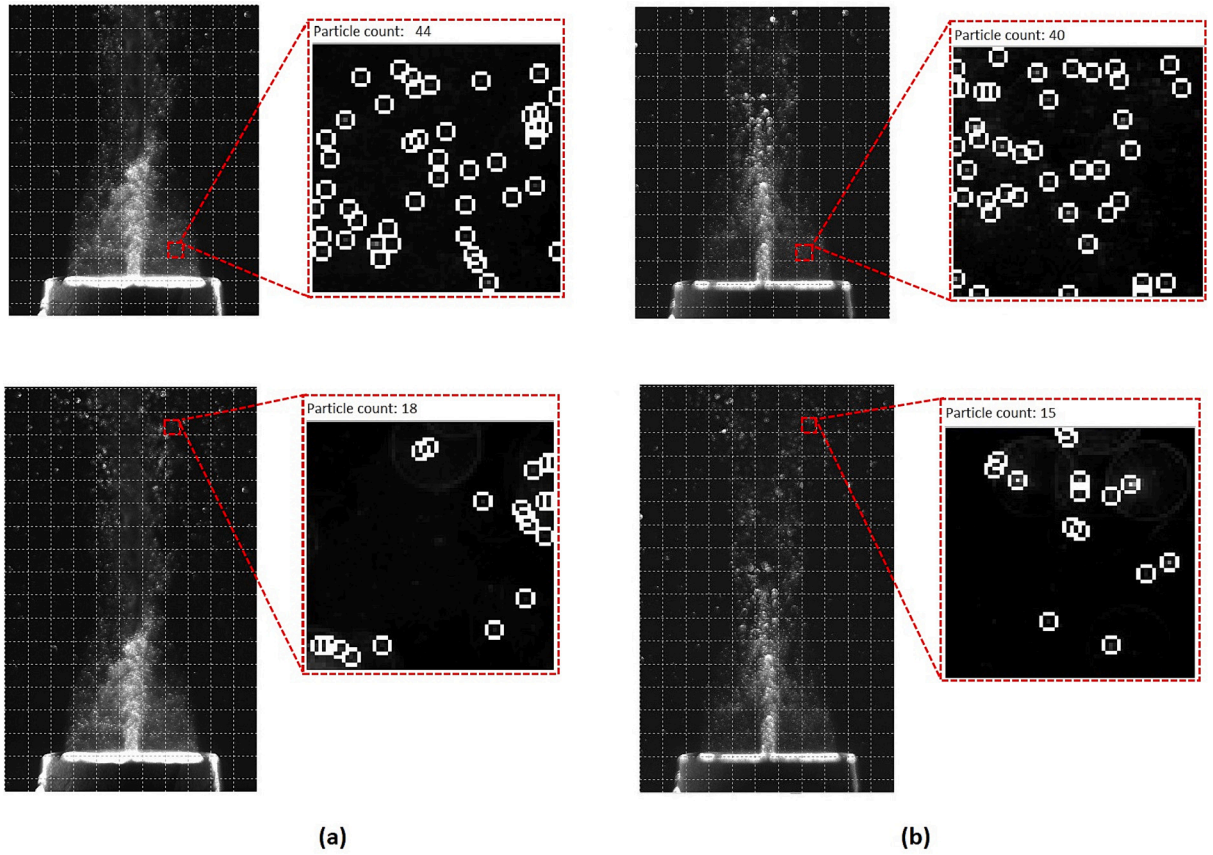

Fig. 4. Comparison of light scattering and particle detection at upstream (close to nozzle exit plane) and downstream locations: (a) jets operated at similar conditions using typical 0.3 μm laser scattering alumina particles and (b) the same jets operated without alumina particles but using pulverised biomass.

traverse system (0.02 mm resolution) was used to horizontally translate the nozzle, whereas, the position of hot-wire probe was precisely set by using a digital vernier-based clamping system (0.01 mm resolution). Each CTA measurement was repeated three times and data were acquired (spatial increments = 0.2 mm) at a sampling frequency of 10 kHz for 2 s. To obtain both non-swirling and swirling flows from the annulus, the tangential and axial air, used to feed the annular flow stream, was varied thereby generating aerodynamic swirl without the use of geometric inserts [33]. The degree of swirl is expressed by a swirl number (S), defined [39] as the ratio of bulk tangential velocity to bulk axial velocity $\left(S = \frac{W_b}{U_b}\right)$. The Reynolds number of the annular jet is defined on the basis of outer radius of annulus R_o and average axial velocity over the annulus U_s, based on the volume flow rate (Q) through the flowmeters and cross-sectional area (A) for the annulus:

$$Re_s = \frac{U_s R_o}{\nu}. \quad (3)$$

Table 1 lists the experimental flow settings pertaining to central jet (air) and annular jet.

2.2. Laser diagnostics

In present work, 2D planar PIV was used to experimentally resolve the velocity field of pulverised biomass-laden turbulent flows as illustrated by the schematic in Fig. 3 and also pictured in the Fig. S1 of Supplementary Materials accompanying this study. The PIV system consists of dual-pulsed Nd: YAG laser (make: Dantec Dynamics) having 200 mJ/pulse energy with an operating wavelength and frequency of 532 nm and 10 Hz, respectively. An optical laser guiding system was employed to achieve a diverging laser sheet of ≈1 mm thickness, focused to pass through the central axis of the nozzle. A double-frame charged-coupled device camera (make: Dantec Dynamics, model: Flow Sense EO 16 M-9) with a maximum resolution of 4920 × 3280 pixels and operated at an image acquisition frequency of 4 Hz, was aligned perpendicular to laser sheet to capture raw instantaneous snapshots. An external synchronizer (make: IDT, model: XS-TH) was used to synchronise camera shutter timing with the dual pulses (laser shots) of the laser. Considering the laser sheet thickness of ≈1 mm, the time between two laser shots was kept at 10 μs, ensuring that biomass particles would not leave the measurement plane in this time duration. For a laser sheet of 1 mm thickness and pulse separation time of 10 μs, biomass particles would need a velocity (out of plane) of over 100 m/s to cross 1 mm thick laser sheet. Whereas in present work, the swirling flow case BF-35BB/4.5CJ-S (0.3) attained a maximum tangential velocity of just 13.6 m/s measured above the annulus and considering that the jets were generally diverging along their length, thus negating any possibility of particles crossing the laser sheet in a given pulse separation time.

2.2.1. Particle seeding

The PIV experiments were primarily designed to visualise and resolve the flow behaviour of dispersed phase by using raw pulverised biomass particles without any additional light scattering tracers. To ensure appropriate light scattering, particle detection (by PIV algorithm), and minimum agglomeration of biomass particles, a comparison was made with standard 0.3-μm de-agglomerated alumina PIV tracers (make: Allied High Tech), as presented in Fig. 4. Under same operating conditions, two equally-sized windows in the upstream (x/D = 0.18, r/D = 0.3) and downstream (x/D = 2.4, r/D = 0.3) of nozzle were considered for comparison. For pulverised biomass-laden flows, in the preliminary testing, it was found that light scattering and particle detection substantially depends on the mass flow rate of biomass ($\dot{m_p}$) and Reynolds number (Re_j) of carrier gas (air) jet. Increasing the values

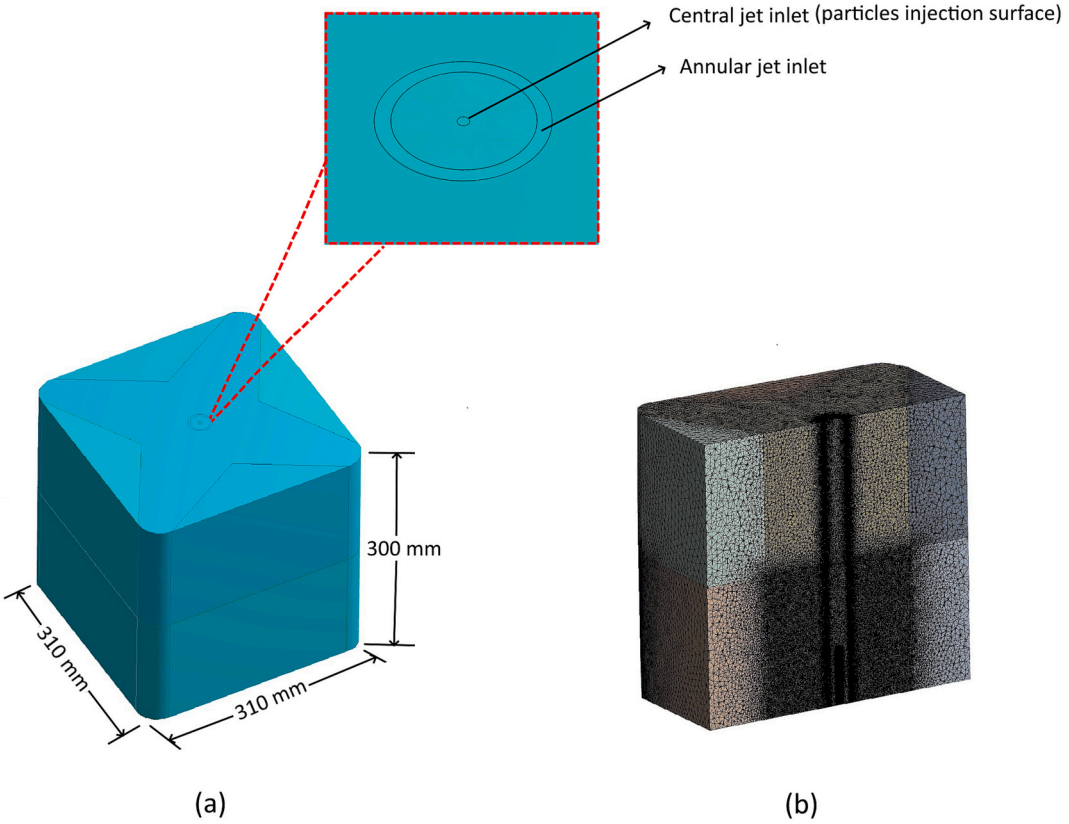

Fig. 5. CFD configuration: (a) 3D fluid domain with detailed view of jet inlets, and (b) sectioned view of multi-body mesh showing regions of fine mesh.

of $\dot{m_p}$ and Re_j beyond certain values caused intense light scattering due to which PIV algorithm could not capture separate particles in the post-processing. On the other hand, lowering the values of aforementioned parameters gave inadequate particle density and transitioned the central jet flow to the laminar regime. Therefore, the values of $\dot{m_p}$ and Re_j were adjusted in such a way to achieve light scattering that does not cause (image) saturation but still allowed particle detection in a turbulent flow regime. The same flow conditions were then repeated for alumina particles and a comparison was made. As depicted in Fig. 4, under same flow settings, biomass particles presented comparable light scattering and particle detection (with minimal agglomeration) relative to that of alumina particles. Beyond these preliminary checks, and for the remainder of experimental test results presented, the pulverised biomass loading and central jet Reynolds number were not varied.

2.2.2. Post-processing

Raw imaging data were acquired and post-processed using Dantec Dynamic Studio 5.1, with these images having a spatial resolution of 0.044 mm/pixel for a field-of-view of 135 mm × 110 mm. For each test condition, Fig. S3 shows that acquiring 500 instantaneous images (at a 4Hz camera frame rate) was sufficient. The PIV data post-processing for present particle-laden flow is based on the methodology described by Göktepe et al. [31] and Birzer et al. [40]. A multi-pass adaptive cross-correlation algorithm [41,42] was used to convert raw PIV images into instantaneous velocity fields. The field-of-view was divided into a fine grid size, i.e. 6 pixels (0.26 mm) and interrogation windows ranging from 8 × 8 pixels (0.35 mm × 0.35 mm) to 16 × 16 pixels (0.7 mm × 0.7 mm) were used for the measurement of instantaneous velocity field. To obtain maximum velocity vectors within the region of interest and attribute a velocity field to the dispersed phase, the grid size and interrogation windows were kept at the smallest possible values. Section S2 of Supplementary Materials describes further details regarding PIV data post-processing and measurement of particle phase velocity field. The accuracy of time-averaged velocity field was ensured by conducting residual error analysis [43] along with the estimation [44,45] of random uncertainty in the PIV measurements, as presented in section S3 and Fig. S3 of Supplementary Materials.

2.3. Numerical approach

2.3.1. Computational domain

To complement the experiments and numerically analyse the influence of particle mass loading and carrier gas turbulence, three dimensional steady-state Reynolds-Averaged-Navier-Stokes (RANS) multiphase (solid-gas) simulations were conducted using ANSYS FLUENT 2020 R1. Fig. 5 presents computational domain with dimensions, multi-phase inlets, and detailed views of mesh, employed in present simulations. A multibody polyhedral mesh comprising of 22.9 million cells with an aspect ratio and orthogonal quality of 1.78 and 0.8, respectively, was used. The regions where high velocity gradients were expected such as shear layers of annular and central jet, were additionally refined relative to other parts of the mesh (Fig. 5b). The mesh independence and uncertainty in the discretization was evaluated using GCI (Grid Convergence Index) based method [46] and discussed in detail elsewhere [36].

2.3.2. Turbulence and dispersed phase models

In present study, the multiphase turbulent flows were modelled by applying Eulerian-Lagrangian approach. For the gas-phase, time-averaged continuity and momentum equations were solved in a Eulerian frame of reference. The dispersed phase (particle phase) was modelled in Lagrangian frame and individual sample particles were tracked. Considering the complexity (anisotropic turbulence and swirling flow) of gas phase flow, Reynolds Stress Model (RSM) was used to compute the closure term for momentum governing equation [47,48]. The selection of RSM was based on the results of authors' previous work [36] where

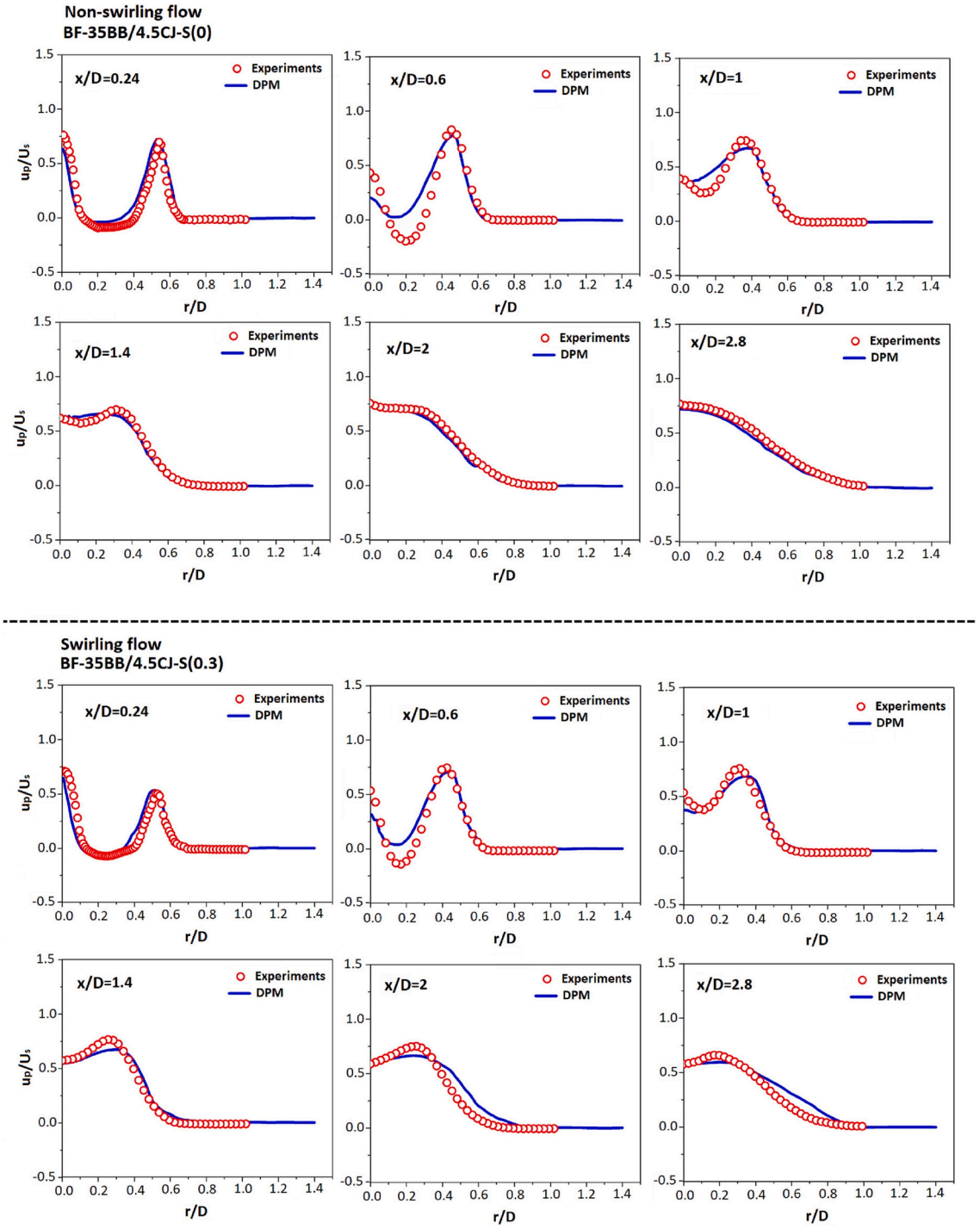

Fig. 6. Model validation for non-swirling and swirling particle-laden flow: validation of radial distribution of mean particle axial velocities obtained from DPM against PIV experiments.

under same geometric configuration and mesh, the viability and accuracy of RSM was compared with other turbulence models and found to be superior. For the particle phase, discrete phase model (DPM) was used to track individual motion of biomass particles and predict time-averaged particle velocities. In DPM, the particle inertia is balanced with the acting forces to track particle motion and trajectories [48] such that:

$$\frac{\partial \overrightarrow{v_p}}{\partial t} = F_D\left(\overrightarrow{v} - \overrightarrow{v_p}\right) + \frac{\overrightarrow{g}\left(\rho_p - \rho\right)}{\rho_p}, \tag{4}$$

where the term $F_D\left(\overrightarrow{v} - \overrightarrow{v_p}\right)$ represents drag force per unit particle mass and $\frac{\overrightarrow{g}\left(\rho_p - \rho\right)}{\rho_p}$ accounts for the effect of gravity on particles. The symbol v_p represents velocity of particle, ρ_p is particle density, v denotes fluid (carrier gas) velocity,and ρ shows the fluid density.

2.3.3. Boundary conditions and solution methods

The gas-phase turbulence model and governing equations were solved using the finite volume method. The SIMPLE algorithm [48] for pressure-velocity coupling and a second-order upwind scheme was

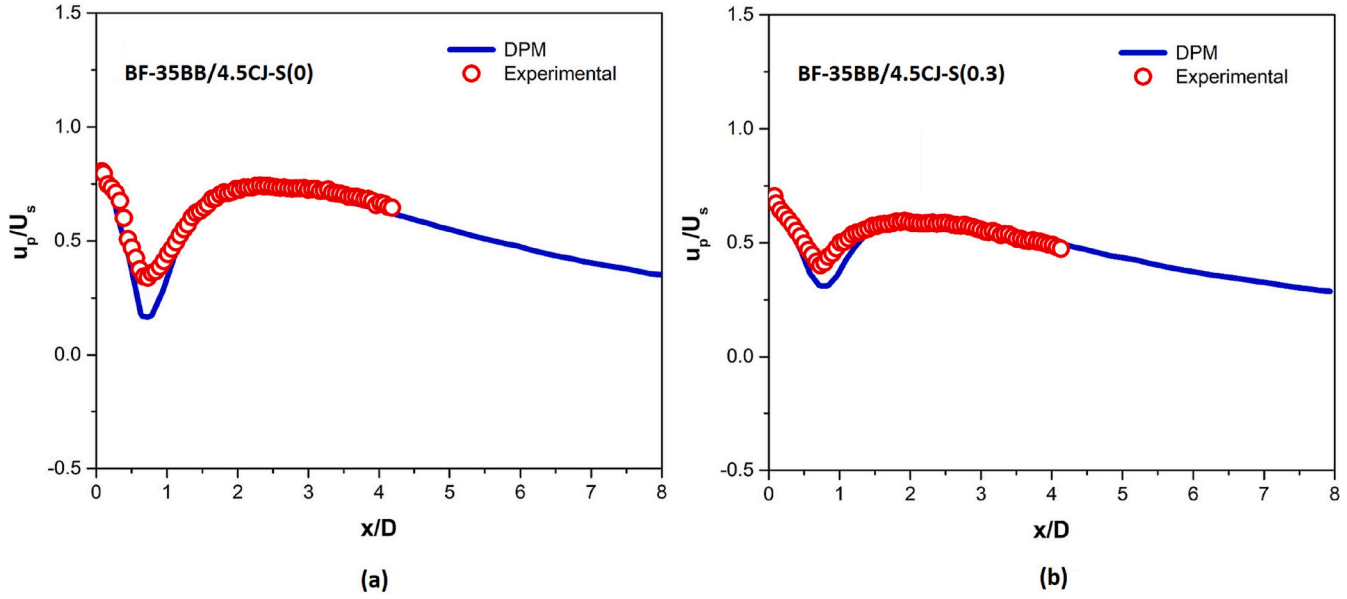

Fig. 7. Centreline mean particle axial velocity comparison between DPM and experimental results.

employed for discretising the convective terms in the transport equations. In terms of boundary conditions, CTA resolved axial and tangential velocity profiles were imposed at the velocity inlets (central jet and annular jet), a no-slip boundary condition was applied on the walls, and far field boundary was designated as a pressure outlet. The interaction of particles with the continuous phase was activated (two-way coupling), and wood particles were selected as materials to reflect the pulverised biomass used throughout the experiments. Numerically, particles were injected from the central jet using surface injection with Rossin-Rammler diameter distribution such that D_{min}, D_{mean} and D_{max} were set to be 5 μm, 40 μm and 150 μm, respectively. Further details regarding selection of Rosin-Rammler distribution parameters are presented in section S4 of the Supplementary Materials. To incorporate and predict the influence of gas phase turbulence on particle motion and dispersion, a discrete random walk stochastic model [48] was implemented. Furthermore, steady-state data sampling was applied on DPM variables to evaluate particle mean characteristics such as mean particle velocity field and volume fraction.

2.3.4. Model validation

To ensure physical representative results and determine the accuracy of DPM predictions, detailed validations against experimental data were carried out for biomass-laden turbulent jets under non-swirling and swirling conditions. Whereas, validation for gas phase predictions and the accuracy of RSM is described in detail elsewhere [36]. Figs. 6 and 7 present the comparison of radial (at various x/D locations) and axial distribution of time-averaged particle axial velocity obtained from PIV and DPM predictions for non-swirling BF-35BB/4.5CJ-S(0) and swirling BF-35BB/4.5CJ-S(0.3) test cases. To produce dimensional independent results, the velocity data (experimental and CFD) were normalised with average axial velocity through the annulus (U_s). It can be observed that DPM presented high levels of accuracy in the extreme upstream region (x/D = 0.24) by accurately capturing particle peak velocity over the central jet and annulus along with the particle flow in shear layer region. Similar to experiments, the particles in simulations were injected only from the central jet and the particle velocity obtained over the annulus was due to those particles which were entrained into the annular jet through the bluff-body stabilised recirculation zones (BBRZ). This validates the viability of DPM in acceptable predictions of central particle-laden jet dispersion into turbulent annular flows. Overall good agreement was found between experiments and DPM at downstream locations except at x/D = 0.6, where a noticeable discrepancy in dispersed phase velocity was observed for both cases (more obvious in non-swirling case). It is evident that the DPM accurately captured the particle flow reversal close to the nozzle exit plane, however it over estimated the annular jet's dissipation (faster jet decay) and mixing with the central particle-laden jet. This resulted in decreased particle velocity in the jet core and over the bluff-body region (Fig. 6). The possible reason for this discrepancy is attributed to an innate limitation of RSM based solutions, i.e. under estimation of gas phase velocity in annular flow geometries (near bluff-body region) [36,48,49]. Since, the annular jet was not seeded with biomass particles, and RSM being responsible for gas phase modelling, there occurred an under predicted upstream gas velocity that resulted in overestimation of annular flow entrainment and diffusion [36]. Additionally, Fig. 7 shows that, except at x/D = 0.6–0.8, DPM accurately predicted centreline particle velocities without any

Table 2
Test cases for experimental and numerical analyses.

Experimental cases	Description	Particles	S	Re_s	Re_j
BF-4.5CJ	Particle-laden central jet only	Bark flour (BF)	–	–	4500
BF-35BB/4.5CJ-S(0)	BB annular jet + Particle-laden central jet		0	35,500	
BF-35BB/4.5CJ-S(0.3)			0.3		
Numerical cases	**Description**	$\dot{m_p}$**(kg/s)**	$\dot{m_a}$**(kg/s)**	Φ_p	**Re_j**
N-35BB/4.5CJ-S(0)	Benchmark case (S = 0)	4.73×10^{-5}	1.44×10^{-4}	0.33	4500
N-35BB/4.5CJ-S(0.3)	Benchmark case (S = 0.3)	4.73×10^{-5}	1.44×10^{-4}	0.33	4500
N(1.75$\dot{m_a}$)-35BB/7.8CJ-S(0.3)	75% increase in $\dot{m_a}$	4.73×10^{-5}	2.52×10^{-4}	0.19	7800
N(0.43$\dot{m_p}$)-35BB/4.5CJ-S(0.3)	43% decrease in $\dot{m_p}$	2.71×10^{-5}	1.44×10^{-4}	0.19	4500

Key: BF: bark flour; CJ: central jet; BB: bluff-body; N: numerical; S: swirl number; Re_s: Reynolds number of annular jet; Re_j: Reynolds number of central jet; $\dot{m_p}$: mass flowrate of particles; $\dot{m_a}$: mass flowrate of air; Φ_p: particle loading ratio.

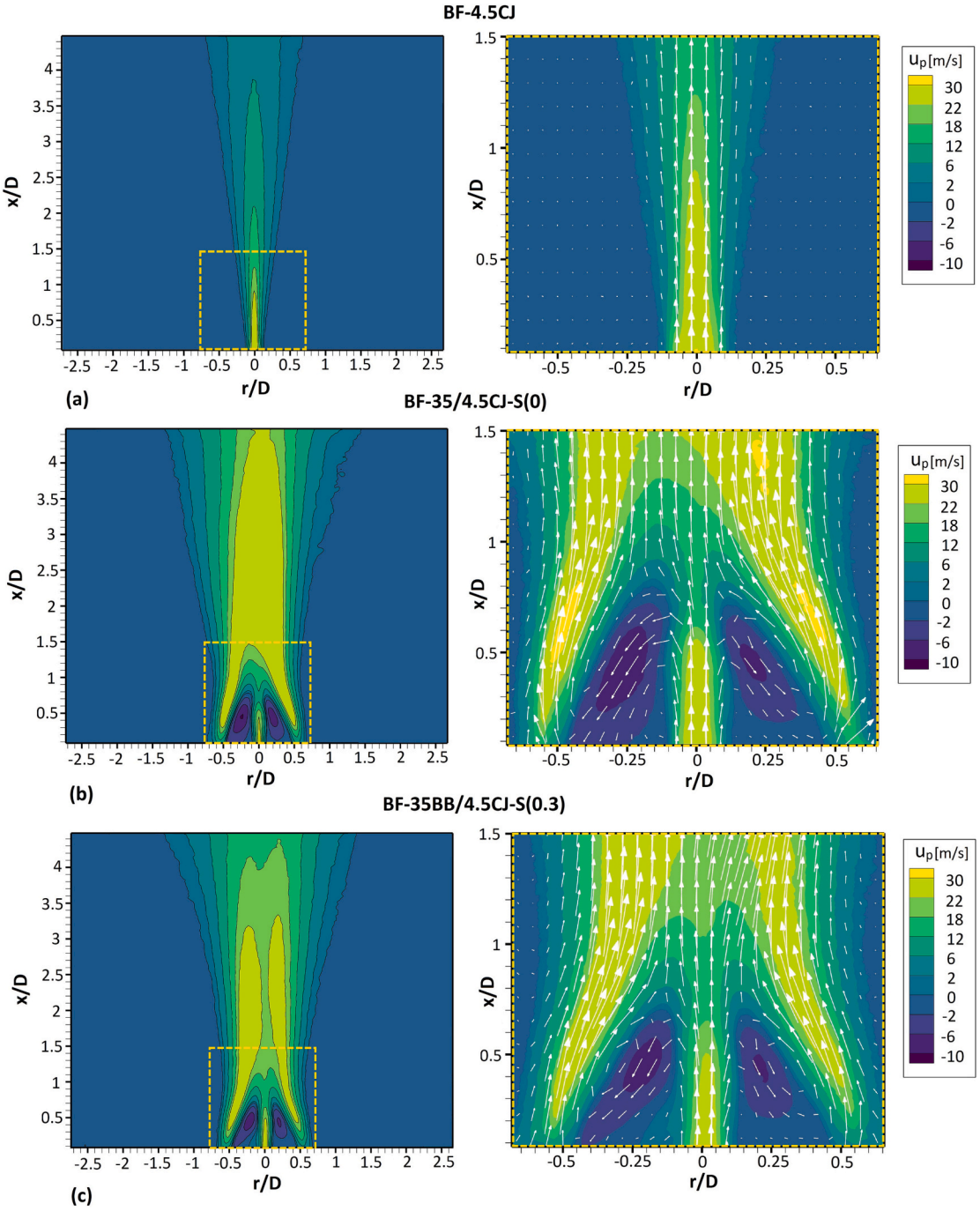

Fig. 8. Mean particle axial velocity contour maps with corresponding upstream directional vectors: (a) BF-4.5CJ, (b) BF-35BB/4.5CJ-S(0) and (c) BF-35BB/4.5CJ-S(0.3).

distinguishable uncertainty throughout the flow domain. In terms of turbulence parameters, Fig. S5 of the Supplementary Materials presents validations for non-swirling and swirling flow test cases. Comparison of mean particle axial fluctuating velocity shows good agreement between experimental and numerical results, particularly for BF-35BB/4.5CJ-S (0.3) case.

3. Results and discussion

Table 2 presents details pertaining to experimental and numerical test cases of present work investigating pulverised biomass-laden turbulent jets as stand-alone and when subjected to turbulent annular jets (non-swirling and swirling).

Experiments were conducted for three cases:

i. A baseline case featuring a stand-alone pulverised biomass-laden turbulent central jet, case **BF-4.5CJ,**
ii. The addition of a non-swirling turbulent annulus to (i), case **BF-35BB/4.5CJ-S(0),** and
iii. Further increasing the flow complexity of (ii) by adding swirl to the turbulent annulus, case **BF-35BB/4.5CJ-S(0.3)**.

Further insights are then obtained through numerical simulations employing multi-phase modelling into the particle dispersion characteristics when achieved through varying the flow rate of carrier gas or particle loading. All numerical cases are prefixed with the "N"

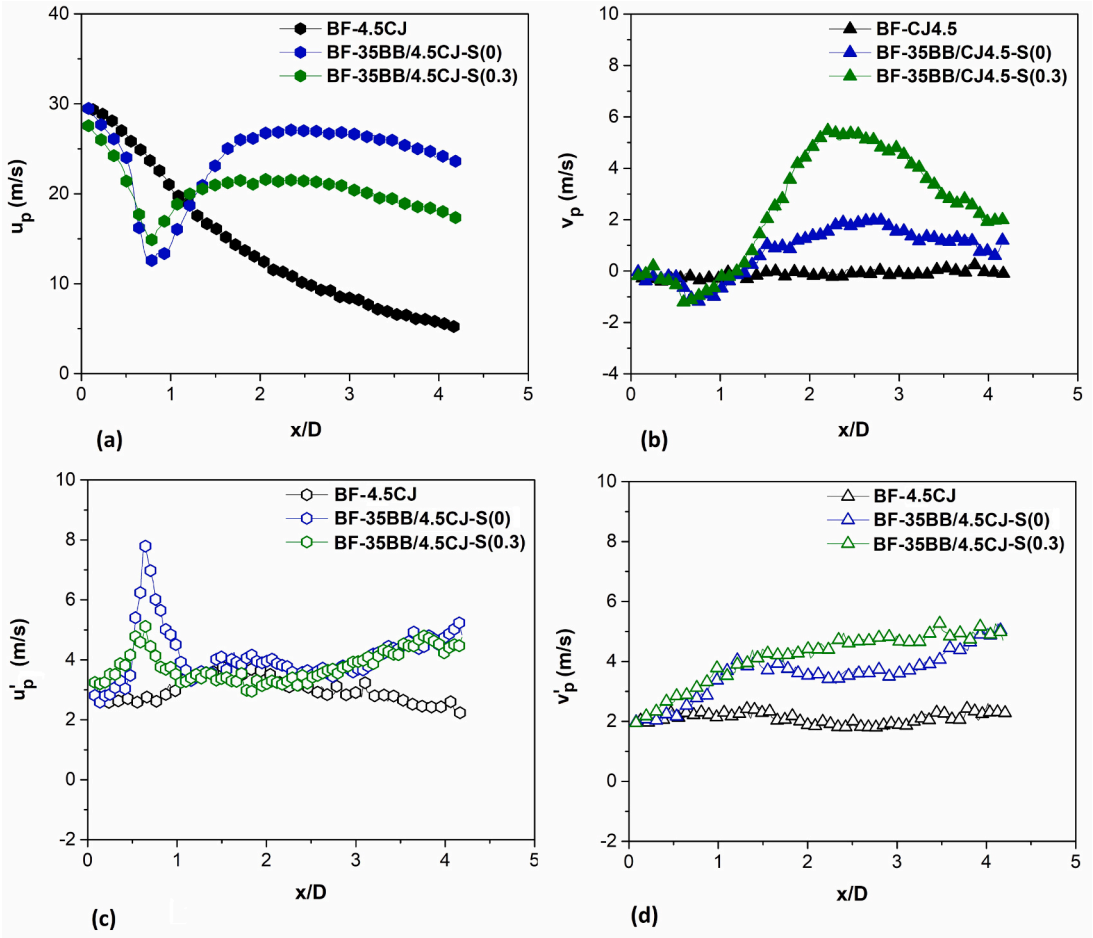

Fig. 9. Axial (x/D = 0) distribution of mean particle velocities with their respective fluctuating velocities in a central jet BF-4.5CJ and when subjected to both non-swirling (S = 0) and swirling (S = 0.3) conditions: (a) particle axial velocity, (b) particle radial velocity, (c) particle axial fluctuating velocity and (d) particle radial fluctuating velocity.

designator:

i. Baseline conditions used for model validation against the experimental conditions tested (ii and iii), cases **N-35BB/4.5CJ-S(0)** and **N-35BB/4.5CJ-S(0.3),**
ii. Increases of 75% to the carrier gas' Reynolds number compared to the experiments conducted in (iii), case **N(1.75$\dot{m_a}$)-35BB/7.8CJ-S(0.3),** and
iii. Decreases by 43% to the (powder) loading of pulverised biomass compared to the experiments conducted in (iii), case **N(0.43$\dot{m_p}$)-35BB/4.5CJ-S(0.3)**.

3.1. *Underlying particle-laden flow dynamics*

Fig. 8a and b illustrate the dispersed phase flow-field for a pulverised biomass-laden central jet, when operated stand-alone BF-4.5CJ or subjected to an additional non-swirling annulus BF-35BB/4.5CJ-S(0), respectively. Analysis of velocity contours and directional vectors reveals a strong interaction of annular jet with the biomass-laden central jet. The gas phase annular jet develops its characteristic flow feature around the periphery of central jet and in the immediate wake of bluff-body, known as bluff-body based recirculation zone (BB-RZ) [51,52]. The detailed flow characteristics of gaseous annular jet and BB-RZ are well described in authors previous work [35]. The BB-RZ plays a crucial role in the recirculation and dispersion of biomass particles over the bluff-body and downstream of the flow, respectively. When biomass-laden central jet interacts with the BB-RZ, the strongly recirculating vortices picks up biomass particles from the central jet, recirculate them over the bluff-body and then disperse downstream of the flow (Fig. 8b). It is worth mentioning that only central jet was seeded with pulverised biomass particles, no PIV tracers or additional seeding from the annulus were applied, therefore the flow contours and directional vectors are solely representative of flow and dispersion behaviour of pulverised biomass particles. To add further clarity, Fig. S6(a) of Supplementary Materials shows three dimensional CFD simulations conducted for N-BF-35BB/4.5CJ-S(0) and N-BF-35BB/4.5CJ-S(0.3) cases. Analysis of predicted particle trajectories clearly shows that the particles originally ejected from the central jet were picked up by the annular jet, recirculated inside the BB-RZ and then ultimately dispersed in the downstream. In terms of pulverised biomass combustion in annular geometries (non-premixed combustion), the BB-RZ would act as a stabilising mechanism for biomass-laden jet to promote fuel-oxidiser mixing as well as help complete combustion of biomass particles by recirculating and retaining them within the reaction zone. To quantify the interaction of pulverised biomass-laden jet with a turbulent annular jet, axial distribution (at r/D = 0) of mean particle velocity and turbulent fluctuating velocities for BF-4.5CJ and BF-35BB/4.5CJ-S(0) are shown in Fig. 9. Whereas Fig. 10 presents radial distribution of mean particle velocity (axial, radial) data at various x/D positions. The influence of annular jet in BF-35BB/4.5CJ-S(0) on the particle-laden central jet starts to appear at x/D ≈ 0.64, where with respect to a central jet only as in case BF-4.5CJ, the centreline mean particle axial velocity (u_p) exhibits a sudden dip (35% decrease) with a corresponding sharp hike (177% increase) in the

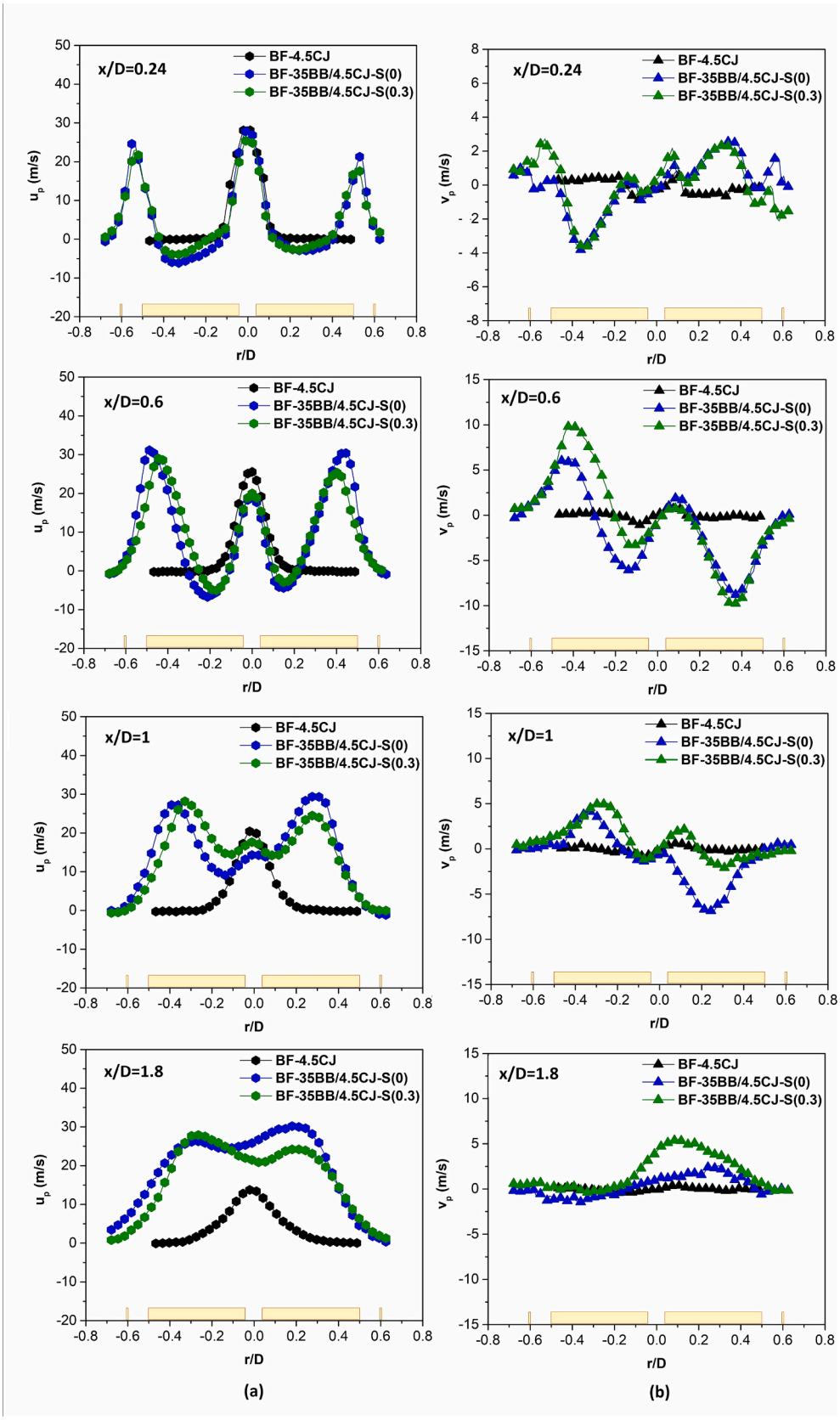

Fig. 10. Radial distribution of mean particle velocities at various upstream locations in a central jet BF-4.5CJ and when subjected to both non-swirling (S = 0) and swirling (S = 0.3) conditions: (a) mean particle axial velocity and (b) mean particle radial velocity.

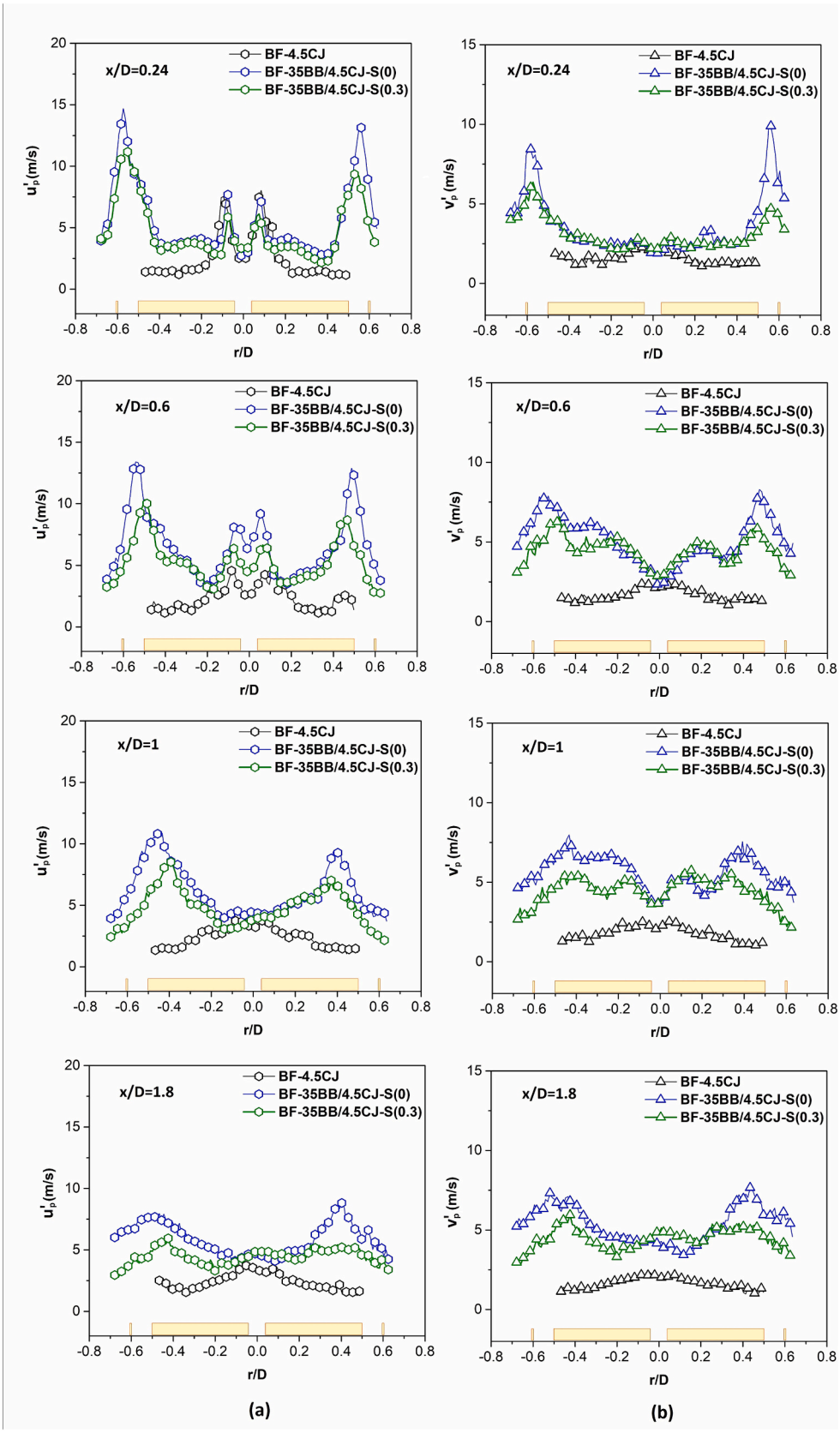

Fig. 11. Radial distribution of mean particle fluctuating velocities at various upstream locations: (a) mean particle axial fluctuating velocity and (b) mean particle radial fluctuating velocity.

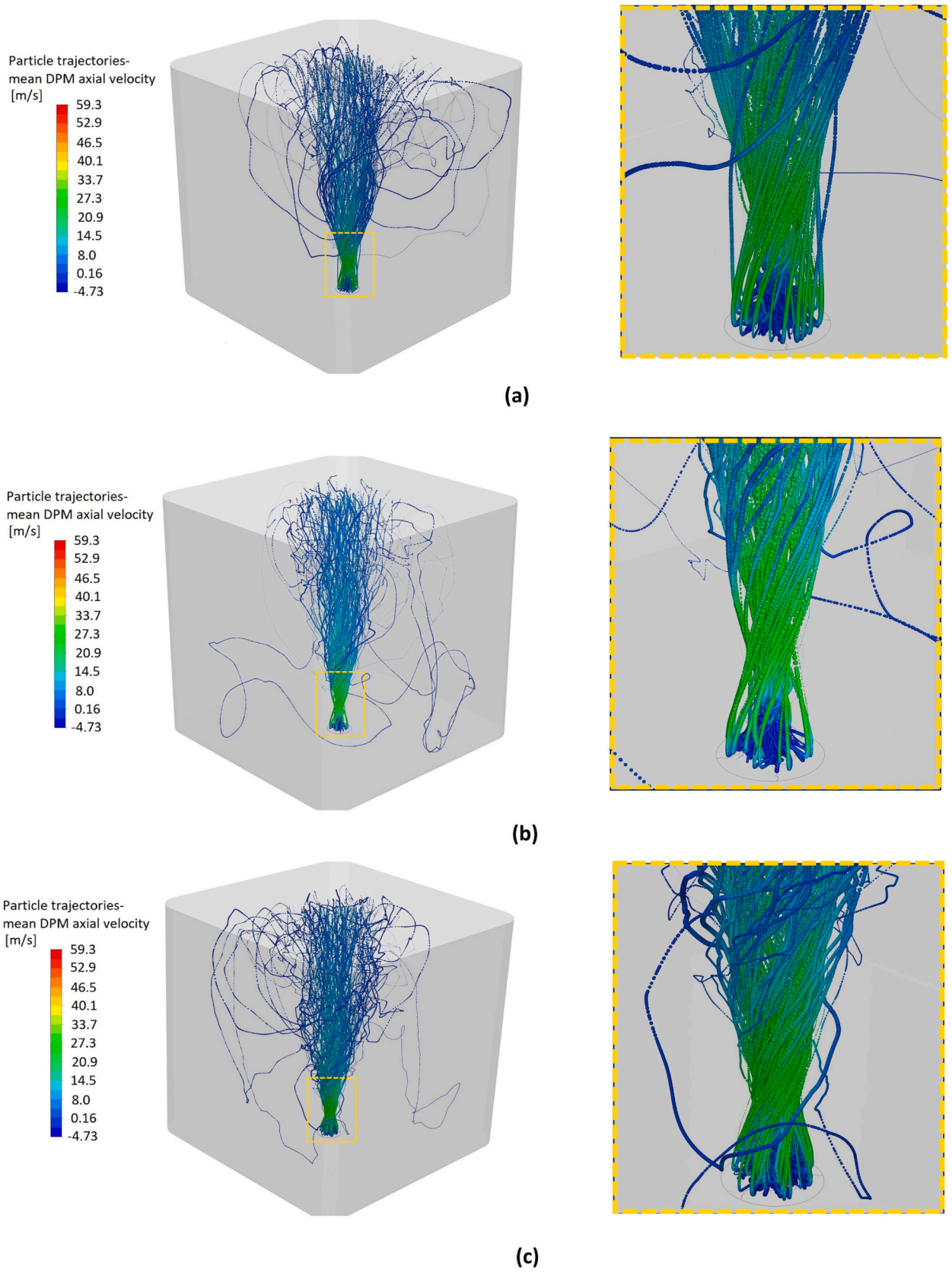

Fig. 12. Mean particle trajectories for axial velocity: (a) N-35BB/4.5CJ-S(0.3), (b) N(1.75$\dot{m}_a$)-35BB/7.8CJ-S(0.3) and (c) N(0.43$\dot{m}_p$)-35BB/4.5CJ-S(0.3).

particle axial fluctuating velocity ($u_p^{'}$) (Fig. 9a and c). This is because when biomass-laden central jet (with positive axial momentum) impinges into the strongly recirculating (having negative axial momentum) BB-RZ, turbulence increases drastically causing the particle velocity to drop and initiate mixing of two streams. To further resolve this turbulence, radial distribution (at various upstream x/D positions) of mean particle axial and radial fluctuating velocities are presented in Fig. 11. It was found that for BF-35BB/4.5CJ-S(0) at x/D = 0.6 and in the shear layer region of central jet, the $u_p^{'}$ shows a 96.3% increase compared to that of BF-4.5CJ, thus reinforcing the previous observation of intense turbulence and enhanced mixing in this upstream region at x/D ≈ 0.6–0.7. Similarly, the interaction of biomass particles with BB-RZ can also be observed in the radial distribution of mean particle axial velocity (Fig. 10a, x/D = 0.6), where 35BB/4.5CJ-S(0) shows a 24.3% decrease (relative to BF-4.5CJ) in the peak value of u_p (at r/D = 0) with particles strongly recirculating in BB-RZ at a negative velocities of −4 to −6 m/s at r/D = ±0.1 to ±0.3. Fig. 9a shows that entrainment of the biomass-laden central jet (into the annular jet) starts from x/D ≈ 1.2 in case BF-35BB/4.5CJ-S(0). Furthermore, as the axial location x/D = 1.8 is approached, the central jet also appears to completely diffuse with its peak being totally consumed by the annular jet as depicted in Fig. 10a, x/D = 1.8. An asymmetry can be observed in particle axial velocities at x/D = 1 and 1.8, which is attributed to the underlying intrinsic asymmetric gas phase annular flow [35].The entrainment of particle-laden jet is further resolved by analysing the axial distribution of mean particle radial velocity (v_p) in Fig. 9b in case BF-35BB/4.5CJ-S(0). A gradual increase can be observed in v_p starting from x/D ≈ 1.2 and reaching a maximum value of 1.85 m/s at x/D = 2.6 (at this location BF-4.5CJ shows almost negligible v_p). This manyfold increase in particle radial velocity indicates that annular jet, in addition to retaining biomass particles in the BB-RZ, significantly disperses the particles downstream of the flow as shown in Fig. 9b for case BF-35BB/4.5CJ-S(0). In addition to this, it is also evident in Fig. 10 from the radial distribution of v_p that biomass particles attains significant radial velocities once they start recirculating in the BB-RZ as occurs with case BF-35BB/4.5CJ-S(0) This flow behaviour of raw pulverised bark flour proves its viability (as a fuel) in non-premixed combustion, where dispersion and diffusion of fuel jet (biomass-laden) into the surrounding oxidiser (annular jet) critically affects overall combustion performance and emissions.

3.2. Impact of swirl on particle flow and turbulence field

The introduction of swirl to a turbulent annular flow generally imparts additional flow complexities such as imparting rotary motion to BB-RZ, high levels of turbulence and certain characteristic flow features (vortex breakdown) [20,52]. To resolve the effect of swirl on the pulverised biomass particle flow and dispersion characteristics, mean particle velocity and turbulence data are discussed in this section. Analysis of particle axial velocity contours and vectors for swirling flow BF-35BB/4.5CJ-S(0.3) (Fig. 8c) shows overall identical results compared to its non-swirling counterpart BF-35BB/4.5CJ-S(0) (Fig. 8b) in terms of particle interaction with BB-RZ and swirling annulus. However, as expected, addition of swirl significantly enhanced the downstream radial dispersion of the biomass particles. Comparison of mean particle trajectories presented in Fig. S6a and S6b shows that swirling annular flow N-BF-35BB/4.5CJ-S(0.3) picks up significantly more biomass particles, relative to N-BF-35BB/4.5CJ-S(0) from the central jet, imparts swirl motion to these particles and then disperses them further downstream in the largely quiescent surrounding flow domain formed by the enclosure. Keeping in mind that the same number of biomass particles were injected in both numerical cases, however the particle trajectories of N-BF-35BB/4.5CJ-S(0.3) case clearly show larger lateral spread and dispersion relative to N-BF-35BB/4.5CJ-S(0) (Fig. S6a,b). This increased lateral spreading can be attributed to the centrifugal forces associated with swirling flows [54]. The influence of swirl on biomass particles can further be resolved by analysing the axial distribution of mean particle axial and radial velocity (Fig. 9) in case BF-35BB/4.5CJ-S(0.3). It can be seen that similar to non-swirling case BF-35BB/4.5CJ-S(0), an upstream at x/D ≈ 0.64 a dip in the particle axial velocity with a corresponding increase in particle axial fluctuating velocity was observed (Fig. 9a,c). However, this reduction in u_p and increase in $u_p^{'}$ is 9.3% and 34% less, respectively, as compared to the non-swirling case BF-35BB/4.5CJ-S(0). The reason for this difference between non-swirling and swirling cases is attributed to the structure of the BB-RZ. It is well established from the literature that a BB-RZ for swirling annular flow can be open at the centre (positive velocity at the centre) [56] while it's closed (with a stagnation point) for the non-swirling flow [35,51,53,54,55]. Therefore, when biomass-laden jet impinges into a closed BB-RZ (non- swirling case), particles interacts with the strong negative velocity that generates higher turbulence (steep hike in $u_p^{'}$) and causes significant reduction in u_p as compared to that of opened BB-RZ (swirling case) where particles at the centre interact with positive gas velocity and generates relatively low turbulence. The comparison of radial distribution of mean particle axial fluctuating velocity of BF-35BB/4.5CJ-S(0) and BF-35BB/4.5CJ-S (0.3) shows that swirl has negligible effect on the shear layer turbulence of central biomass-laden jet except at x/D = 0.6 (Fig. 11a). Similarly, the radial fluctuating velocity ($v_p^{'}$) also remains identical for non-swirling and swirling cases over the region of biomass-laden central jet and its corresponding shear layer region. In addition to this, the entrainment of biomass-laden central jet into swirling annular flow starts at x/D ≈ 1.2 which is identical to the non-swirling case BF-35BB/4.5CJ-S(0)). The particle axial velocity gradually starts increasing, however the value of u_p remains significantly less (20% at x/D = 2.2) than that of BF-35BB/4.5CJ-S(0) case (Fig. 9a). This reduction in centreline particle axial velocity is attributed to swirling annular jet (gas phase) decay. The swirling flows are always associated to faster jet decay and rapid shear layer growth (compared to non-swirling flow) due to their highly turbulent nature, better convective transport and entrainment characteristics [54,57]. Furthermore, the faster decay of particle axial velocity in case BF-35BB/4.5CJ-S(0.3) is counterbalanced by a rise in particle radial velocity, as shown in Fig. 9b. The radial particle velocity for BF-35BB/4.5CJ-S(0.3) starts rising from x/D ≈ 1.2 and reaches to a maximum value of 5.2 m/s at x/D = 2.2, which is 254% greater than that of non-swirling case BF-35BB/4.5CJ-S(0). Göktepe et al. [31] reported similar increasing trends of particle radial velocity (increased lateral spreading) with swirl intensity for pulverised pine particles. These significant differences between non-swirling BF-35BB/4.5CJ-S(0) and swirling BF-35BB/4.5CJ-S(0.3) cases validates the substantial role of swirl in rapid axial diffusion (faster jet decay) of biomass-laden jet with a corresponding downstream lateral dispersion.

3.3. Impact of carrier gas and particle mass flow rates

In addition to pulverised biomass-laden flow experiments, three dimensional multiphase CFD simulations were conducted to model pulverised biomass-laden jet in a confined turbulent swirling annular flow. Parametric analysis was conducted to predict resultant particle flow and dispersion characteristics by varying the particle loading ratio (with respect to benchmark case) using two criteria, i.e. decreasing biomass loading or increasing Reynolds number of the carrier gas (air jet carrying particles). The numerical test cases were designed in such a way that the mass flow rate of biomass particles ($\dot{m_p}$) and mass flow rate of air ($\dot{m_a}$) was decreased by 43% in N($0.43\dot{m_p}$)-35BB/4.5CJ-S(0.3) and increased by 75% in N($1.75\dot{m_a}$)-35BB/7.8CJ-S(0.3), respectively, while particle loading ratio (Φ_p) was kept same for both cases as shown in Table 2. The results of numerical test cases are compared with each other and as a reference with the benchmark case N-35BB/4.5CJ-S(0.3). Fig. 12 presents 3D visualisation of mean particle trajectories for the benchmark case and test cases. Comparison of N($0.43\dot{m_p}$)-35BB/4.5CJ-S (0.3) and N($1.75\dot{m_a}$)- 35BB/7.8CJ-S(0.3) shows that for the same value

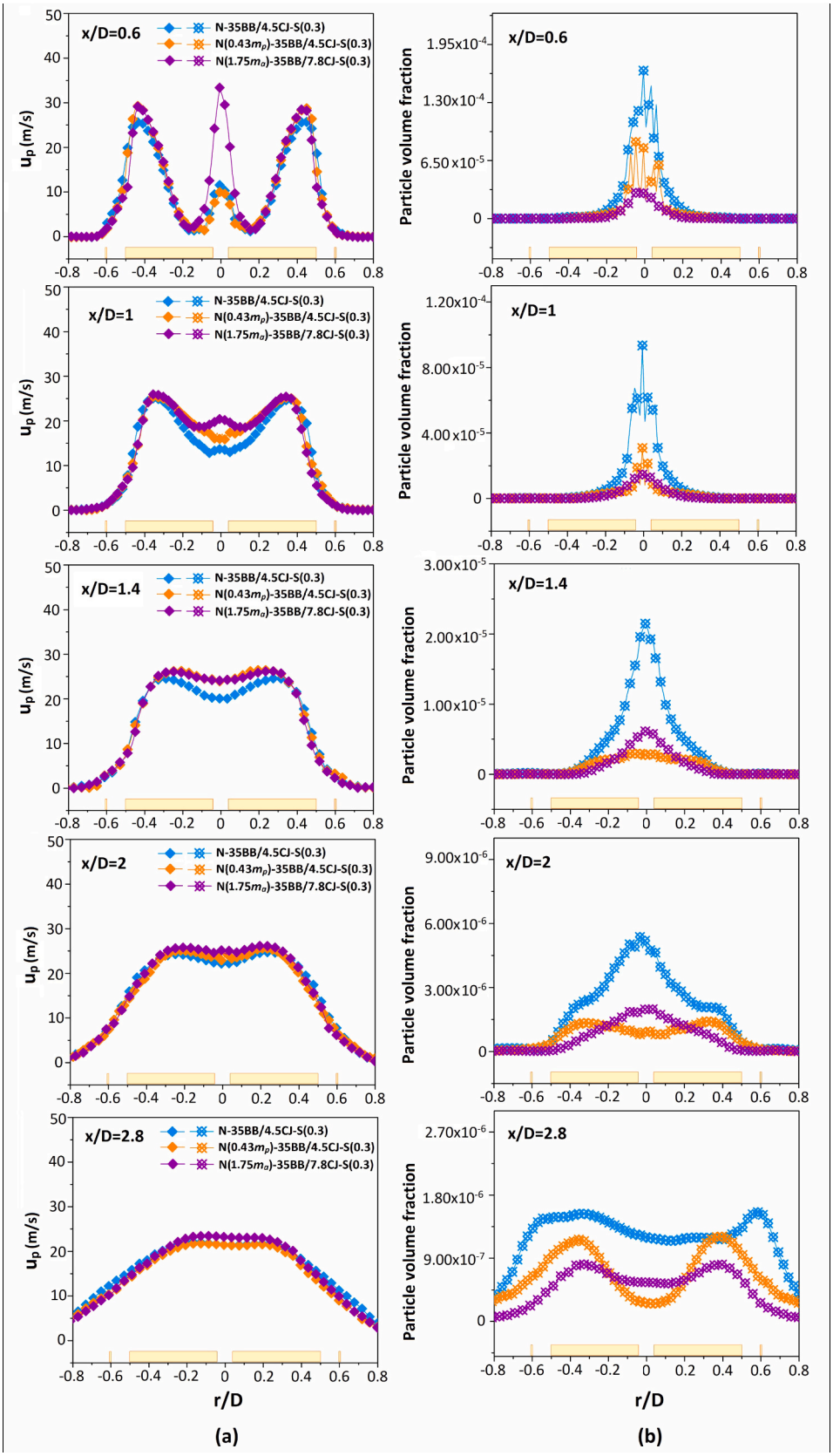

Fig. 13. Radial distribution of predicted mean particle velocity and volume fraction at various x/D locations: (a) mean particle axial velocity and (b) mean particle volume fraction.

of Φ_p, increasing the Reynolds number of carrier gas from $Re_j = 4500$ to $Re_j = 7800$ reduces biomass particle recirculation inside the BB-RZ as shown in Fig. 12b,c. This is because the high axial momentum of central jet restricts the annular jet to penetrate into and pick up biomass particles rather it forces the majority of the particles to escape the flow domain without being recirculated in the BB-RZ. Whereas, for of case N($0.43\dot{m_p}$)-35BB/4.5CJ-S(0.3), it can be seen that not only more particles lies inside the BB-RZ but the overall effect of swirl motion is also more pronounced as compared to case N($1.75\dot{m_a}$)-35BB/7.8CJ-S(0.3) (Fig. 12c). Furthermore, biomass particles under the strong influence of swirling annulus also improves downstream particle dispersion for N($0.43\dot{m_p}$)-35BB/4.5CJ-S(0.3), as evident from the lateral spread of particle trajectories in Fig. 12c. To further support, particle trajectories, radial distribution of mean particle axial velocity and volume fraction (predicted via DPM) at various x/D locations are presented in Fig. 13. It can be seen that from x/D = 0.6 to x/D = 1 (upstream of nozzle), for case N($0.43\dot{m_p}$)-35BB/4.5CJ-S(0.3), the peak of volume fraction of biomass particles is greater than that of N($0.43\dot{m_p}$)-35BB/4.5CJ-S(0.3) and lies over the central jet region (r/D = −0.1 to 0.1). At the axial location just beyond the BB-RZ from x/D = 1.4 and x/D = 2, the volume fraction of N($0.43\dot{m_p}$)-35BB/4.5CJ-S(0.3) grows radially and shows two peaks at r/D ≈ 0.4 and − 0.4 leaning towards the annulus as compared to the single and relatively narrow peak of N($1.75\dot{m_a}$)-35BB/7.8CJ-S(0.3) as shown in Fig. 13b. This indicates relatively higher biomass particle concentration in the reattachment region of annular jet for N($0.43\dot{m_p}$)-35BB/4.5CJ-S(0.3) compared to N($1.75\dot{m_a}$)-35BB/7.8CJ-S(0.3). Similarly, further downstream at x/D = 2.8, it can be seen that for almost identical mean particle velocities (Fig. 13a), the volume fraction of N($0.43\dot{m_p}$)-35BB/4.5CJ-S(0.3) shows a higher peak with larger radial spread (from r/D ≈ 0.6 to −0.6) than to N($1.75\dot{m_a}$)-35BB/7.8CJ-S(0.3) which just start to have two peaks at r/D ≈ 0.4 and − 0.4 (Fig. 13b). These observations can be summarised as for the same particle loading ratio of two test cases, the biomass volume fraction of N($0.43\dot{m_p}$)-35BB/4.5CJ-S(0.3) shows a relatively higher downstream growth with lateral expansion, which supports previous observations from mean particle trajectories (Fig. 12c) that relatively low Reynolds number of carrier gas allows annular jet to pick up more particles from the central jet and results in increased downstream dispersion of biomass particles. Finally, from the comparison of particle trajectories and volume fraction data of test cases with the benchmark case, it can be deduced that when particle loading ratio is reduced from 0.33 to 0.19, the case N($0.43\dot{m_p}$)-35BB/4.5CJ-S(0.3) performs better than N($1.75\dot{m_a}$)-35BB/7.8CJ-S(0.3) in terms of biomass particles recirculation, downstream dispersion and overall entrainment into the annular flow.

4. Conclusions

Time-averaged two-dimensional planar PIV experiments along with three-dimensional multiphase RANS simulations (DPM based) have been conducted to investigate pulverised raw biomass (bark flour) laden turbulent jet ($Re_j = 4500$ and 7800) flow and dispersion characteristics. Analyses are conducted first on stand-alone particle-laden jet and then under confined turbulent annular flows ($Re_s = 35{,}500$) at non-swirling (S = 0) and swirling (S = 0.3) conditions. The numerical predictions are based on well-resolved (via CTA) boundary conditions and validated against PIV data. The conclusions of this work are summarised below:

- **Underlying particle-laden flow dynamics:** Pulverised raw biomass-laden jet strongly impinges into the BB-RZ of turbulent annular jet. The biomass particles are well picked up by strong vortices of BB-RZ, recirculated over the bluff-body and then dispersed downstream of the flow (validated by mean particle trajectories). A 35% decrease and 177% increase in the mean particle axial velocity and turbulent fluctuation is recorded respectively, indicating intense upstream (x/D ≈ 0.64) turbulent mixing and effective particle dispersion into the BB-RZ. In terms of downstream entrainment, annular jet completely engulfs pulverised biomass-laden at x/D = 1.8.
- **Impact of swirl on particle flow and turbulence field:** In case of swirling annular flow, a relatively weaker interaction with pulverised biomass-laden jet takes place that results in a 34% decrease in upstream turbulence compared to non-swirling case. This reduction in turbulence is attributed to the underlying structure of BB-RZ of swirling annular flow. Despite this, addition of swirl to annular flow significantly enhances the downstream dispersion and lateral spread of biomass particles as evident from the 20% and 254% massive increase (compared to non-swirling case) in mean particle axial and radial velocities, respectively.
- **Impact of carrier gas and particle mass flow rates:** In terms of CFD simulations, particle loading ratio is reduced from 0.33 to 0.19 via two different criteria, i.e. Increasing the Reynolds number of carrier gas and decreasing the biomass particle loading (with same Reynolds number). It is concluded that, for a constant particle loading ratio, the test case having relatively low Reynolds number of carrier gas allows better particle recirculation (promote mixing) in BB-RZ and enhances downstream lateral dispersion and entrainment of biomass-laden jet compared to high Reynolds number case.

CRediT authorship contribution statement

Syed Ehtisham Gillani: Conceptualization, Methodology, Investigation, Data curation, Visualization, Software, Formal analysis, Writing – original draft. **Yasir M. Al-Abdeli:** Conceptualization, Methodology, Writing – review & editing, Supervision. **Zhao F. Tian:** Conceptualization, Methodology, Writing – review & editing, Supervision.

Declaration of Competing Interest

The authors declare that they have no known competing financial interests or personal relationships that could have appeared to influence the work reported in this paper.

Data availability

Data will be made available on request.

Acknowledgements

The corresponding author acknowledges the Higher Education Commission (HEC) Pakistan and Edith Cowan University (ECU) Australia for the award of HEC-ECU PhD scholarship.

Appendix A. Supplementary data

Supplementary data to this article can be found online at https://doi.org/10.1016/j.powtec.2023.118855.

References

[1] D. Kunii, O. Levenspiel, Circulating fluidized-bed reactors, Chem. Eng. Sci. 52 (15) (1997) 2471–2482.
[2] H. Shalaby, K. Wozniak, G. Wozniak, Numerical calculation of particle-laden cyclone separator flow using LES, Eng. Appl. Comp. Fluid Mech. 2 (4) (2008) 382–392.
[3] A. Tremel, D. Becherer, S. Fendt, M. Gaderer, H. Spliethoff, Performance of entrained flow and fluidised bed biomass gasifiers on different scales, Energy Convers. Manag. 69 (2013) 95–106.
[4] M. Zhao, A.I. Minett, A.T. Harris, A review of techno-economic models for the retrofitting of conventional pulverised-coal power plants for post-combustion capture (PCC) of CO 2, Energy Environ. Sci. 6 (1) (2013) 25–40.
[5] M. Balat, G. Ayar, Biomass energy in the world, use of biomass and potential trends, Energy Sources 27 (10) (2005) 931–940.
[6] A. Demirbas, Combustion characteristics of different biomass fuels, Prog. Energy Combust. Sci. 30 (2) (2004) 219–230.

[7] D. Nordgren, H. Hedman, N. Padban, D. Boström, M. Öhman, Ash transformations in pulverised fuel co-combustion of straw and woody biomass, Fuel Process. Technol. 105 (2013) 52–58.
[8] A. Williams, M. Pourkashanian, J. Jones, Combustion of pulverised coal and biomass, Prog. Energy Combust. Sci. 27 (6) (2001) 587–610.
[9] Y.M. Al-Abdeli, A.R. Masri, Stability characteristics and flowfields of turbulent non-premixed swirling flames, Combust. Theory Model. 7 (4) (2003) 731.
[10] S.R. Gubba, et al., Numerical modelling of the co-firing of pulverised coal and straw in a 300MWe tangentially fired boiler, Fuel Process. Technol. 104 (2012) 181–188.
[11] Á.D.G. Llamas, N. Guo, T. Li, R. Gebart, K. Umeki, Rapid change of particle velocity due to volatile gas release during biomass devolatilization, Combust. Flame 238 (2022), 111898.
[12] A. Elfasakhany, L. Tao, B. Espenas, J. Larfeldt, X.-S. Bai, Pulverised wood combustion in a vertical furnace: experimental and computational analyses, Appl. Energy 112 (2013) 454–464.
[13] A. Elorf, et al., Effect of swirl strength on the flow and combustion characteristics of pulverized biomass flames, Combust. Sci. Technol. 191 (4) (2019) 629–644.
[14] G. Lu, Y. Yan, S. Cornwell, M. Whitehouse, G. Riley, Impact of co-firing coal and biomass on flame characteristics and stability, Fuel 87 (7) (2008) 1133–1140.
[15] F. Tabet, I. Gökalp, Review on CFD based models for co-firing coal and biomass, Renew. Sust. Energ. Rev. 51 (2015) 1101–1114.
[16] A.A. Bhuiyan, A.S. Blicblau, A.S. Islam, J. Naser, A review on thermo-chemical characteristics of coal/biomass co-firing in industrial furnace, J. Energy Inst. 91 (1) (2018) 1–18.
[17] M. Alletto, M. Breuer, One-way, two-way and four-way coupled LES predictions of a particle-laden turbulent flow at high mass loading downstream of a confined bluff body, Int. J. Multiphase Flow 45 (2012) 70–90.
[18] S. Angriman, P.D. Mininni, P.J. Cobelli, Velocity and acceleration statistics in particle-laden turbulent swirling flows, Phys. Rev. Fluids 5 (6) (2020), 064605.
[19] F. Liang, J. Zhang, H. Zhang, Gas and particle instantaneous velocity measurement in swirling particle-laden turbulent reacting flow, Powder Technol. 395 (2022) 360–368.
[20] Y.M. Al-Abdeli, A.R. Masri, Recirculation and flowfield regimes of unconfined non-reacting swirling flows, Exp. Thermal Fluid Sci. 27 (5) (2003) 655–665.
[21] A. Masri, P. Kalt, Y. Al-Abdeli, R. Barlow, Turbulence–chemistry interactions in non-premixed swirling flames, Combust. Theory Model. 11 (5) (2007) 653–673.
[22] J. Dai, S. Sokhansanj, J.R. Grace, X. Bi, C.J. Lim, S. Melin, Overview and some issues related to co-firing biomass and coal, Can. J. Chem. Eng. 86 (3) (2008) 367–386.
[23] Q. Guo, X. Chen, H. Liu, Experimental research on shape and size distribution of biomass particle, Fuel 94 (2012) 551–555.
[24] J. Capecelatro, O. Desjardins, An Euler–Lagrange strategy for simulating particle-laden flows, J. Comput. Phys. 238 (2013) 1–31.
[25] L. Brandt, F. Coletti, Particle-laden turbulence: progress and perspectives, Annu. Rev. Fluid Mech. 54 (2022) 159–189.
[26] C. Fang, J. Xu, H. Zhao, W. Li, H. Liu, Experimental investigation on particle entrainment behaviors near a nozzle in gas–particle coaxial jets, Powder Technol. 286 (2015) 55–63.
[27] M. Xu, J. Yuan, C. Han, C. Zheng, Investigation of particle dynamics and pulverized coal combustion in a cavity bluff-body burner, Fuel 74 (12) (1995) 1913–1917.
[28] L.G. Becker, S. Pielsticker, B. Böhm, R. Kneer, A. Dreizler, Particle dynamics in a gas assisted coal combustion chamber using advanced laser diagnostics, Fuel 269 (2020), 117188.
[29] R. Yan, Z. Chen, B. Zhang, Y. Zheng, Z. Li, Impact of radial air staging on gas-particle flow characteristics in an industrial pulverized coal boiler, Energy 243 (2022), 123123.
[30] A. Elorf, et al., Swirl motion effects on flame dynamic of pulverized olive cake in a vertical furnace, Combust. Sci. Technol. 188 (11–12) (2016) 1951–1971.
[31] B. Göktepe, A.H. Saber, R. Gebart, T.S. Lundström, Cold flow experiments in an entrained flow gasification reactor with a swirl-stabilized pulverized biofuel burner, Int. J. Multiphase Flow 85 (2016) 267–277.
[32] C. Geschwindner, K. Westrup, A. Dreizler, B. Böhm, Pulse picking of a fiber laser enables velocimetry of biomass-laden jets at low and ultra-high repetition rates, in: Proceedings of the Combustion Institute, 2022. In Press.
[33] Y.M. Al-Abdeli, A.R. Masri, Review of laboratory swirl burners and experiments for model validation, Exp. Thermal Fluid Sci. 69 (2015) 178–196.
[34] Z. Wan, S. Yang, D. Tang, H. Yuan, J. Hu, H. Wang, Particle-scale modeling study of coaxial jets of gas-solid swirling flow in an industrial-scale annular pipe via CFD-DEM, Powder Technol. 419 (2023), 118307.
[35] S.E. Gillani, Y.M. Al-Abdeli, Experiments into the interaction of side dilution jets with bluff-body stabilised annular jets, Exp. Thermal Fluid Sci. 146 (2023), 110906.
[36] S.E. Gillani, Y.M. Al-Abdeli, Z.F. Tian, Effect of side dilution jets on the velocity field and mixing in swirl and bluff-body stabilised annular confined flows, Proc. Inst. Mech. Eng. Part A J. Power Energy 237 (2) (2023) 365–384.
[37] M. Di Giacinto, F. Sabetta, R. Piva, Two-Way Coupling Effects in Dilute Gas-Particle Flows, 1982.
[38] Z.U. Ahmed, Y.M. Al-Abdeli, F.G. Guzzomi, Corrections of dual-wire CTA data in turbulent swirling and non-swirling jets, Exp. Thermal Fluid Sci. 70 (2016) 166–175.
[39] Y.M.A. Al-Abdeli, Experiments in Turbulent Swirling Non-premixed Flames and Isothermal Flows, Doctoral Dissertation, School of Aerospace, Mechanical and Mechatronic Engineering, University of Sydney, 2004.
[40] C. Birzer, P. Kalt, N. Smith, G. Nathan, Particle image velocimetry in the near field of a particle-laden precessing jet flow, in: Proceedings of the 4th Australian Conference on Laser Diagnostics in Fluid Mechanics and Combustion, ACLDFMC, 7–9 December, 2005, pp. 21–24.
[41] M. Raffel, C.E. Willert, J. Kompenhans, Particle Image Velocimetry: A Practical Guide, Springer, 1998.
[42] S. DantecDynamicsA, DynamicStudio user's Guide, Dantec Dynamics, Skovlunde, 2013.
[43] J. Stafford, E. Walsh, V. Egan, A statistical analysis for time-averaged turbulent and fluctuating flow fields using particle image velocimetry, Flow Meas. Instrum. 26 (2012) 1–9.
[44] R.J. Adrian, Particle-imaging techniques for experimental fluid mechanics, Annu. Rev. Fluid Mech. 23 (1) (1991) 261–304.
[45] A. Prasad, R. Adrian, C. Landreth, P. Offutt, Effect of resolution on the speed and accuracy of particle image velocimetry interrogation, Exp. Fluids 13 (2) (1992) 105–116.
[46] I.B. Celik, U. Ghia, P.J. Roache, C.J. Freitas, Procedure for estimation and reporting of uncertainty due to discretization in CFD applications, J. Fluids Eng. Trans. ASME 130 (7) (2008).
[47] A.M. Jawarneh, G.H. Vatistas, Reynolds Stress Model in the Prediction of Confined Turbulent Swirling Flows, 2006.
[48] A. Fluent, Ansys Fluent Theory Guide vol. 15317, Ansys Inc., USA, 2011, pp. 724–746.
[49] A. Brito Lopes, N. Emekwuru, B. Bonello, E. Abtahizadeh, On the highly swirling flow through a confined bluff-body, Phys. Fluids 32 (5) (2020), 055105.
[51] B.B. Dally, D.F. Fletcher, A.R. Masri, Flow and mixing fields of turbulent bluff-body jets and flames, Combust. Theory Model. 2 (2) (1998) 193–219.
[52] M. Vanierschot, E. Van den Bulck, Influence of swirl on the initial merging zone of a turbulent annular jet, Phys. Fluids 20 (10) (2008), 105104.
[53] Y.M. Al-Abdeli, A.R. Masri, Precession and recirculation in turbulent swirling isothermal jets, Combust. Sci. Technol. 176 (5–6) (2004) 645–665.
[54] A.K. Gupta, D.G. Lilley, N. Syred, Swirl Flows, Tunbridge Wells, 1984.
[55] A. Danlos, G. Lalizel, B. Patte-Rouland, Experimental characterization of the initial zone of an annular jet with a very large diameter ratio, Exp. Fluids 54 (2013) 1–17.
[56] M. Percin, M. Vanierschot, B.V. Oudheusden, Analysis of the pressure fields in a swirling annular jet flow, Exp. Fluids 58 (2017) 1–13.
[57] T. Park, V. Katta, S. Aggarwal, On the dynamics of a two-phase, nonevaporating swirling jet, Int. J. Multiphase Flow 24 (2) (1998) 295–317.